IEEE Access
Multidisciplinary | Rapid Review | Open Access Journal

Received November 21, 2018, accepted December 13, 2018, date of publication December 20, 2018,
date of current version January 11, 2019.

Digital Object Identifier 10.1109/ACCESS.2018.2888928

Retrieval of Ionospheric Faraday Rotation Angle in Low-Frequency Polarimetric SAR Data

YIFEI JI[1], (Student Member, IEEE), YONGSHENG ZHANG[1], QILEI ZHANG[1], ZHEN DONG[1], AND BAIDONG YAO[2]

[1]College of Electronic Science, National University of Defense Technology, Changsha 410073, China
[2]East China Research Institute of Electronic Engineering, China Electronics Technology Corporation, Hefei 230031, China

Corresponding authors: Yongsheng Zhang (zyscn@163.com) and Qilei Zhang (zhangqilei@nudt.edu.cn)

This work was supported in part by the International Science and Technology Cooperation Program (ISTCP) of China under Grant 2015DFA10270 and in part by the National Natural Science Foundation of China (NSFC) under Grant 61501477 and Grant 61171123.

ABSTRACT A low-frequency spaceborne synthetic aperture radar (SAR) working system, e.g., operating at the *L*-band or *P*-band, has great advantages of military target detection and biomass monitoring. Nevertheless, it is more susceptible to ionospheric effects compared with the higher frequency system. A trans-ionospheric wave propagation model is established in this paper to incorporate ionospheric effects on SAR signals. As one of the significant distortion sources for the polarimetric SAR (PolSAR), Faraday rotation (FR) is mainly imposed by background ionosphere, and its spatial variation is discussed. FR estimators have been devised in succession to estimate FR angle (FRA), and various potential novel estimators can still be derived. But, from a viewpoint of theoretical expressions, the earliest estimator is bound to be the optimal one. Based on PolSAR real data, this mathematical conclusion is further validated via comprehensive performance analysis as to estimation bias and standard deviation rather than the existent root-mean-square principle. Finally, a step-by-step procedure of the FRA map is proposed and operated with an application of the airborne P-band PolSAR data. In particular, the ambiguity error of FRA estimates within a SAR observation is simulated and resolved. By processing the ALOS-2 real data, the spatial distribution of FRAs is retrieved and used to operate ionospheric total electron content soundings.

INDEX TERMS Spaceborne synthetic aperture radar (SAR), Faraday rotation (FR) estimators, FR angle (FRA) map, ionospheric TEC soundings.

I. INTRODUCTION

There has been a burgeoning trend in the development of the spaceborne L-band or P-band synthetic aperture radar (SAR) system, for realizing foliage and subsurface penetration; it has potential advantages of investigating military targets, monitoring soil moisture or retrieving global biomass [1]–[3]. The L-band missions have been already in-operation, e.g. the Advanced Land Observing Satellite (ALOS) Phased Array Type L-band Synthetic Aperture Radar (PALSAR) and its follow-on mission of ALOS-2 [4], [5]. Fortunately, a free archive with abundant PALSAR data has become available for our research and thereby relevant real data processing has come true. Furthermore, the spaceborne P-band SAR mission called Biomass that aims at forest coverage observation and global biomass measurements is put on agenda by European Space Agency (ESA). However, these low-frequency missions may be significantly influenced by ionospheric impacts, including dispersion, phase advance, group delay, Faraday rotation (FR), and scintillation [6]–[10]. It is well known that the total electron content (TEC) is a key parameter to describe ionospheric status, which indicates the integration of electron density along the propagation path. The unit of TEC (TECU) is 10^{16} electrons/m^2.

In particular, a radio signal propagating through the ionosphere experiences a rotation angle of the polarization vector. That is the FR phenomena, a significant distortion source for the polarimetric SAR (PolSAR) application [11]–[17]. It will differentiate the cross-polarized echoes, enhance the like-to-cross-polarized correlation and blend in polarized terms [15]. The FR angle (FRA) is inversely proportional to the square frequency so that the FR effect becomes more significant for the low-frequency case; at solar maximum, the one-way FRA can arrive at as large as 40 degrees at L-band and 321 degrees at P-band [13]–[15]. The polarimetric distortions induced by ionospheric perturbations within the azimuth integrated time can be neglected for the most cases [12]. Therefore, due to the

probable spatial variation of the ionospheric TEC [8], FRAs across a SAR image tend to exhibit a spatial-variable distribution. Furthermore, in addition to the essential variation of the background ionosphere, the slant TEC (STEC) varying from close to far swath is an important factor to introduce variable components in FRA, which has not yet been recognized in published researches.

The FR influence on the polarimetric scattering matrix has been modeled by using measured scattering matrix, including effects of the system noise, channel imbalance and crosstalk [12]–[16]. FR estimators have been proposed in succession [11], [15], [18]–[21] and employed to mitigate the FR effect [22]–[26]. However, there are still a lot of potential novel estimators we can derive from the measured scattering matrix. It seems difficult to operate performance analysis for multiple estimators to determine the optimal one. From a viewpoint of the signal intensity of mathematical expressions, theoretical analysis can be adopted as an assistant reference in this paper. Based on the selected published FR estimators, comprehensive performance analysis will be carried out to validate this mathematical conclusion. The estimation sensitivity to other polarimetric perturbations will be investigated via estimation bias and standard deviation (STD) rather than the existent root-mean-square (RMS) principle in [19] and [20].

Relevant approaches have been presented to eliminate the ambiguity error of FRA, such as using calibrated scatterers or specific surface characteristics [15], phase unwrapping [18] and FR prediction [21]. In existence of the system noise, the first approach is in general unpractical without the calibrated targets or specific terrain identities [15]. Phase unwrapping is applicable for the FRA distribution in a global scale [18], but it is invalid for a random SAR image. FR prediction has been regarded as the most effective approach [21], but the potential pixel-level ambiguity within a SAR image should be further addressed especially for the P-band mission [22].

Meyer *et al.* gave an example that sizable FRA variations could be retrieved from a typical PALSAR data obtained near the magnetic north pole, where ionospheric fluctuations were intensive by choice [23]. It was the substantial variation of the background ionosphere that introduced FRA fluctuations. In fact, it is a peculiar condition for a PALSAR full-polarimetric data to contain considerable FRA structures due to its narrow observation swath. For the FRA map in PALSAR data, small FRA variations will be sheltered by system noise. In contrast, it is much easier to contain sizable spatial-variable FRA components for the future P-band mission with more sensitivity to ionospheric fluctuations or for the ALOS-2 system with a wider swath. Furthermore, the effectiveness and accuracy of the FRA illustration were not considered in [23]. Therefore, it will be further validated by using airborne P-band PolSAR data, and an intractable condition with the ambiguity error is simulated and addressed. The FRA mapping for the ALOS-2 data will be also performed to retrieve FRA spatial variations mainly introduced by the varying STEC between near and far observation. Subsequently, the retrieved FRA map is applied to mapping STEC or TEC, which is an alternative approach to sounding local ionospheric status.

This paper is organized as follows. It starts with a detail establishment of the wave propagation model in the ionosphere in Section II. A basic description of FRA is given in Section III, where FR prediction and the spatial distribution of FRA are also discussed. In Section IV, published FR estimators are introduced and realized by the real data processing. And their estimation performance is evaluated at first via mathematical expressions to determine the optimal one and then verified by comprehensive performance analysis. An improved strategy of the FRA map is proposed in Section V with consideration of the FRA ambiguity error, and a simulation on basis of the airborne P-band PolSAR data is to confirm the effectiveness of the FRA map. In addition, by utilizing ALOS-2 data, a real data processing example is given to map FRA or ionospheric TEC. Finally, conclusions are summarized in Section VI.

II. WAVE PROPAGATION MODEL IN THE IONOSPHERE

Ionospheric effects on the propagating electromagnetic wave are essentially due to the perturbation of the refractive index, which can be derived by the Appleton-Hartree expression [7]. It is assumed that the signal frequency is not lower than very high frequency (VHF), and thereby the ionospheric refractive index can be approximated as

$$n_i \approx 1 - X\left(1 \mp Y\cos\Theta\right)/2, \tag{1}$$

with

$$\begin{aligned} X &= \omega_p^2/\omega^2, \\ Y &= \mu_0 He/m\omega, \end{aligned} \tag{2}$$

where $\omega_p = \left(N_e e^2/m\varepsilon_0\right)^{1/2}$ and ω are the plasma angular and wave frequencies, μ_0 and ε_0 are the magnetic permeability and dielectric constants in the vacuum, m and e are the mass and charge of an electron, N_e is the ionospheric electron density, $B = \mu_0 H$ is the local magnetic flux density, and Θ is the angle between the propagation normal and geomagnetic field. If the electric field vector of an electromagnetic wave is established as $\mathbf{E} = \mathbf{E}_0 e^{-j\mathbf{k}_0\cdot\mathbf{r}}$ with $\mathbf{E}_0 = \left[E_{0H}\ E_{0V}\right]^T$, it indicates the initial status of the Jones vector, in which $\mathbf{r}$ is the spatial vector and $\mathbf{k}_0$ is the propagation wavenumber with $k_0 = |\mathbf{k}_0| = \omega\sqrt{\mu_0\varepsilon_0}$ in the vacuum. Shown as $\mp$ in Equation (1), the electromagnetic wave entering the ionized medium ($\mathbf{E}_i$) splits into extraordinary and ordinary waves; in detail, a linearly polarized wave is respectively separated into right-handed and left-handed circularly polarized waves with equivalent energy, respectively, which can be expressed as

$$\mathbf{E}_i = \mathbf{E}_L + \mathbf{E}_R = E_L\begin{bmatrix}1\\+j\end{bmatrix} + E_R\begin{bmatrix}1\\-j\end{bmatrix}, \tag{3}$$

with

$$\begin{cases} E_L = \left(E_{0H} - jE_{0V}\right)/2, \\ E_R = \left(E_{0H} + jE_{0V}\right)/2. \end{cases} \tag{4}$$

Then, these two intrinsic polarization signals are propagating with the wavenumber factors of $k_0 n_L$ and $k_0 n_R$, respectively. Once passing through the ionosphere, they recombine into a new linearly polarized wave with a resulting angular deviation relative to the initial direction of the polarization vector [25]. It is supposed that ϕ_L and ϕ_R are the rotation angles of these two circularly polarized waves integrated along the propagation path. Hence, the electric Jones vector of the new wave can be written as

$$\mathbf{E}_i = \mathbf{E}_L e^{j(-k_0 \cdot r + \varphi_i)} e^{j\Omega} + \mathbf{E}_R e^{j(-k_0 \cdot r + \varphi_i)} e^{-j\Omega}, \tag{5}$$

with

$$\varphi_i = \int_s \frac{1}{2} k_0 X ds, \tag{6}$$

$$\Omega = \frac{\phi_L - \phi_R}{2} = \frac{\omega}{2} \int_s (n_L - n_R)\, ds = \int_s \left(\frac{1}{2} XY \cos\Theta \right) ds, \tag{7}$$

where φ_i is the ionospheric phase advance error and Ω is the one-way FRA. Based on (2) and (3), we further obtain [7]

$$\varphi_i = \lambda r_e TEC_s, \tag{8}$$

$$\Omega = KB \cos\Theta \cdot TEC_s \Big/ f^2, \tag{9}$$

where $r_e = e^2 \big/ (4\pi m \varepsilon_0 c^2)$ is the classical radius of an electron, $K = e^3 \big/ (8c\varepsilon_0 m^2 \pi)$ is a constant, c is the light speed in the vacuum, λ is the wavelength, and $f = \omega \big/ 2\pi$ is the signal frequency. The TEC along the SAR slant range is named as STEC. It can be defined as $TEC_s = \int_s N_e ds \approx TEC_\perp \cdot \sec\chi$, where χ is the zenith angle of the ray's penetration into the ionosphere and $TEC_\perp$ is the TEC along the vertical direction, named as VTEC. After further derivation, (5) can be simplified as

$$\mathbf{E}_i = \mathbf{F} \mathbf{E}_0 e^{-jk_0 \cdot r} e^{j\varphi_i}, \tag{10}$$

$$\mathbf{F} = \begin{bmatrix} \cos\Omega & \sin\Omega \\ -\sin\Omega & \cos\Omega \end{bmatrix}. \tag{11}$$

For the strip-map SAR mode, the signal will be transmitted from the antenna, reflected by the scattering target and at last received by the antenna. In this process, it traverses through the ionosphere by twice. Thereby, the received signal can be modeled as

$$\mathbf{E}_r = \mathbf{RFSFTE}_0 e^{-j2k_0 \cdot r} e^{j2\varphi_i}, \tag{12}$$

with

$$\mathbf{S} = \begin{bmatrix} S_{hh} & S_{vh} \\ S_{hv} & S_{vv} \end{bmatrix}, \tag{13}$$

$$\mathbf{R} = \begin{bmatrix} 1 & \delta_1 \\ \delta_2 & f_1 \end{bmatrix}, \quad \mathbf{T} = \begin{bmatrix} 1 & \delta_3 \\ \delta_4 & f_2 \end{bmatrix}, \tag{14}$$

where S_{hh}, S_{hv}, S_{vh} and S_{vv} are the four terms of the scattering matrix $\mathbf{S}$ for a linearly polarized system, $\mathbf{R}$ and $\mathbf{T}$ are the polarimetric distortion matrixes (PDM) of the receiving and transmission system, respectively, $\delta_i, i = 1, 2, 3, 4$ are the four crosstalk terms of polarization channels, and $f_i, i = 1, 2$ are the two channel imbalance elements of the receiving and transmission system. Since this paper emphasizes on the FR effect, other ionospheric effects will not be expanded and the **RFSFT** term in (12) stands for the holistic polarimetric distortion [12]–[15]. Taking the system noise into consideration, the measured scattering matrix $\mathbf{M}$ can be modeled as

$$\mathbf{M} = A\mathbf{RFSFT} + \mathbf{N}, \tag{15}$$

with

$$M = \begin{bmatrix} M_{hh} & M_{vh} \\ M_{hv} & M_{vv} \end{bmatrix}, \quad N = \begin{bmatrix} N_{hh} & N_{vh} \\ N_{hv} & N_{vv} \end{bmatrix} \tag{16}$$

where M_{hh}, M_{hv}, M_{vh} and M_{vv} denote the four elements of the measured scattering matrix, N_{hh}, N_{hv}, N_{vh} and N_{vv} are the channel noise terms, and A is the overall complex gain.

III. FRA

A. FR PREDICTION

It can be observed from (9) that the one-way FRA is inversely proportional to the square frequency. It is also dependent on the local ionospheric and geomagnetic status. The geometric relationship between the geographic (versus geographic east, north, and up directions) and geomagnetic (versus geomagnetic east, north, and up directions) coordinates is illustrated in FIGURE 1, and the unit vector of the geomagnetic field can be transformed into the geographic coordinate and expressed as

$$\mathbf{Q} = \begin{bmatrix} \cos(-I)\sin D & \cos(-I)\cos D & \sin(-I) \end{bmatrix}^T, \tag{17}$$

where I and D are the geomagnetic inclination and declination angles, respectively. One method to accurately obtain Θ is to calculate the propagation vector. It should be presented as $\mathbf{P} = (\mathbf{P}_{tar} - \mathbf{P}_{sat}) \big/ |\mathbf{P}_{tar} - \mathbf{P}_{sat}|$, which is then transformed into the geographic coordinate, and Θ can be calculated by arccos $(\mathbf{P} \cdot \mathbf{Q})$. The another approach is according to an approximation that the orbit inclination is close to 90°, such as the typical sun-synchronous orbits of the ALOS and ALOS-2 satellites. As a result, the propagation

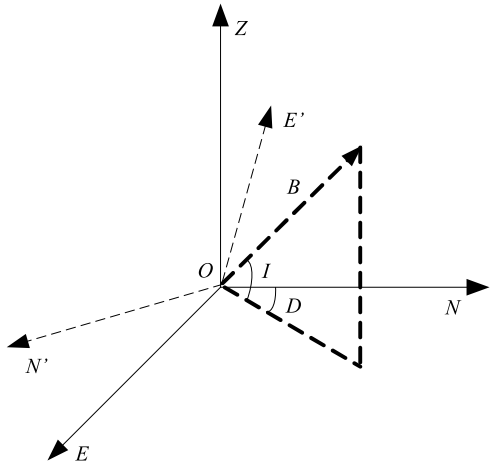

FIGURE 1. Geographic (*O-ENZ*) and geomagnetic (*O-E'N'Z*) coordinates.

vector is also defined in the geographic coordinate, and can be approximated as

$$\mathbf{P} = \begin{bmatrix} \sin\theta_i & 0 & -\cos\theta_i \end{bmatrix}^T, \tag{18}$$

where θ_i is the incident angle at the ionospheric penetration point, generally approaching to the incident angle or the look-down angle for the low Earth orbit (LEO) satellite. Therefore, Θ can be easily calculated by

$$\cos\Theta \approx \cos I \sin D \sin\theta_i + \sin I \cos\theta_i, \tag{19}$$

which is consistent with the expression in [15].

Based on the input parameters, such as longitude, latitude, altitude and time, three primary elements of the geomagnetic field, incorporating geomagnetic inclination, declination and intensity, are obtained by adopting International Geomagnetic Reference Field (IGRF). Furthermore, the TEC values for a given spot and area can be predicted by using International Reference Ionosphere (IRI). Therefore, on basis of the specific SAR geometry and the exterior databases of the ionosphere and geomagnetic field, FRA can be predicted by using (9) as an assistant reference, which is beneficial for the polarization calibration. The FR prediction accuracy has been investigated in [23].

B. FRA SPATIAL DISTRIBUTION

Equation (9) can be rewritten as $\Omega = \sigma \cdot TEC_s$, where $\sigma = KB\cos\Theta/f^2$ is called TEC-to-FRA coefficient. It shows an integral sensitivity of the FRA value to the STEC, which can be calculated by using IGRF. In addition, it is approximately constant in a SAR observation range, but moderately spatial-variable in a global scale. With the incident angle set as 30° and the data set on November 2014, global maps of the TEC-to-FRA versus deg/TECU are illustrated in FIGURE 2. The L-band (1.27 GHz) and P-band (600 MHz) systems are given, respectively shown in FIGURE 2(a) and FIGURE 2(b). The simulation result indicates a notable dependence of the TEC-to-FRA coefficient on the geographic location, and for given STEC variations, it is easier to retrieve spatial distribution of the FRA in the high-latitude regions. In addition, the TEC-to-FRA coefficient of the P-band system is larger than that of the L-band system owing to the dependence on carrier frequency, which implies that it is more probable for the P-band mission to retrieve specific variation components of FRAs.

Within a SAR image scope, FRA fluctuations mainly result from STEC variations, which is involved in the VTEC value and the look-down angle. In terms of the essential distribution of the background ionosphere, it can be generally categorized into two groups: the large-scale and medium-scale distributions [8], [9]. The former is the ionospheric distribution with a macroscopic scale much larger than the image size, leading the holistic homogeneity of the FRA. The latter indicates the medium-scale inhomogeneity of the spatially mild variation with a spatial scale of several kilometers, which is comparable with the image size; thereby it is a potential origin of the spatial-variable FRAs. Another influential element is that the

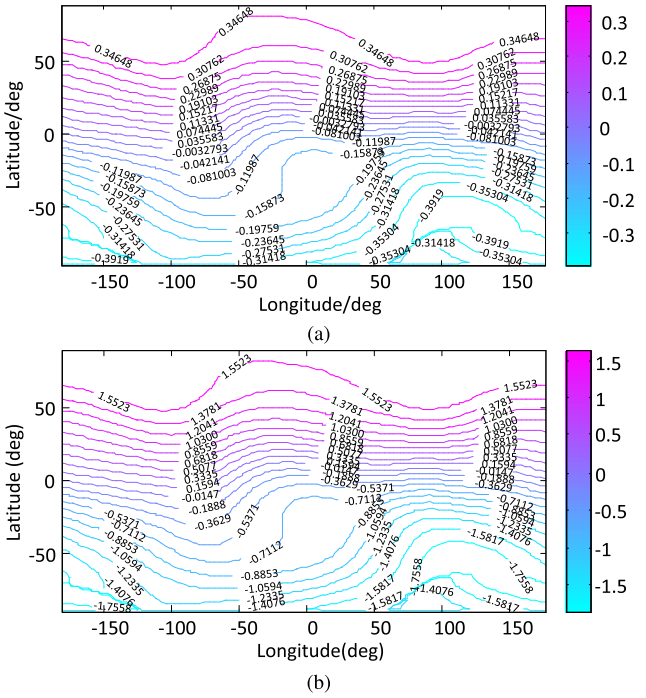

FIGURE 2. Global distributions of TEC-to-FRA (deg/TECU) on Nov. 2014 by using IGRF. (a) At L-band (1270 MHz). (b) At P-band (600 MHz).

propagation path approximates to be linearly variable across the range orientation of the holistic image, which may result in significant differences of FRAs from the close to far swath. Taking these two factors into account, the FRA distribution within a SAR image can be expressed as a function of the pixel location (x, y), which can be given by

$$\Omega(x, y) \approx \sigma \cdot TEC_{\perp}(x, y) \cdot \sec\chi(x, y) \tag{20}$$

IV. FR ESTIMATION IN POLSAR DATA

A. FR ESTIMATORS

It is assumed that FR is the only distortion source due to our focus on FR estimation. Therefore, (15) is simplified as

$$\begin{bmatrix} M_{hh} & M_{vh} \\ M_{hv} & M_{vv} \end{bmatrix} = \begin{bmatrix} \cos\Omega & \sin\Omega \\ -\sin\Omega & \cos\Omega \end{bmatrix} \begin{bmatrix} S_{hh} & S_{vh} \\ S_{hv} & S_{vv} \end{bmatrix} \times \begin{bmatrix} \cos\Omega & \sin\Omega \\ -\sin\Omega & \cos\Omega \end{bmatrix}. \tag{21}$$

Based on the backscatter reciprocity principle ($S_{hv} = S_{vh}$), $\mathbf{M}$ can be expanded as

$$\begin{aligned} M_{hh} &= S_{hh}\cos^2\Omega - S_{vv}\sin^2\Omega, \\ M_{hv} &= S_{hv} - (S_{hh} + S_{vv})\sin(2\Omega)/2, \\ M_{vh} &= S_{hv} + (S_{hh} + S_{vv})\sin(2\Omega)/2, \\ M_{vv} &= S_{vv}\cos^2\Omega - S_{hh}\sin^2\Omega. \end{aligned} \tag{22}$$

Hence, the linear or circular polarimetric covariance matrix (PCM) can be derived from (22), and relevant derivations are attached in the Appendix at the end of the paper. In fact, all of

FR estimators can be derived from the measured polarimetric scattering matrix and the linear or circular PCM.

The Bickle and Bates' estimator, denoted as *B&B*, could be expressed as [11]

$$\Omega_{B\&B} = \frac{1}{4}\arg\left\langle Z_{hv}Z_{vh}^{*}\right\rangle = \frac{1}{4}\arg\left(Y_{23}\right). \tag{23}$$

It can be derived from (38h). And the corresponding term of Y_{23} can be also a function of terms of the linear PCM, which is written as [22]

$$\begin{aligned} Y_{23} = {} & C_{11} - C_{22} - C_{33} + C_{44} + C_{23} + C_{32} + C_{14} + C_{41} \\ & + j(C_{13} + C_{31} + C_{34} + C_{43} - C_{12} + C_{21} \\ & - C_{24} - C_{42}) \end{aligned} \tag{24}$$

Freeman devised two FR estimators, but his first estimator obtained from (22) was an unpractical approach in existence of the system noise [18]. In an attempt to solve this problem, his second estimator (called $F2$) was proposed to make his first one applicable by utilizing spatially averaging approach, which could be described as

$$\Omega_{F2} = \pm\frac{1}{2}\tan^{-1}\sqrt{\frac{\left\langle\left(M_{vh} - M_{hv}\right)\left(M_{vh} - M_{hv}\right)^{*}\right\rangle}{\left\langle M_{hh}M_{hh}^{*}\right\rangle + \left\langle M_{vv}M_{vv}^{*}\right\rangle + 2Re\left\langle M_{hh}M_{vv}^{*}\right\rangle}}, \tag{25}$$

Chen proposed six FR estimators according to (36b)-(36f) and (36h)-(36l); the third and sixth estimators, respectively abbreviated as *Ch*3 and *Ch*6, proved to have better robustness than the others and could be given by [19]

$$\Omega_{Ch3} = \frac{1}{2}\arg\left[Im\left(C_{14}\right) + jIm\left(C_{13}+C_{34}-C_{12}-C_{24}\right)/2\right], \tag{26}$$

$$\Omega_{Ch6} = \frac{1}{2}\arg\left[Im\left(C_{12}+C_{13}-C_{34}-C_{24}\right)/2 - jIm\left(C_{23}\right)\right]. \tag{27}$$

According to the the assumption of the azimuth reflection symmetry, described as $O_{12} = O_{13} = O_{24} = O_{34} = 0$, two estimators were proposed [20], *Li*1 and *Li*2 for short, which could be written as

$$\Omega_{Li1} = \frac{1}{2}\arg\left[\left(C_{11}-C_{44}\right)+jRe\left(C_{13} + C_{24} - C_{12} - C_{34}\right)\right], \tag{28}$$

$$\Omega_{Li2} = \frac{1}{2}\arg\left[Re\left(C_{12} + C_{24}+C_{13}+C_{34}\right) + j\left(C_{22} - C_{33}\right)\right], \tag{29}$$

In premise of the reflection symmetry principle, Wang also proposed an FR estimator, $W1$ for short, which was derived from (38b)-(38e) and (38i)-(38l), and could be presented as [21]

$$\Omega_{W1} = \frac{\arg\left(Y_{12} + Y_{34}\right) - \arg\left(Y_{13} + Y_{24}\right)}{4}. \tag{30}$$

However, all of the above FR estimators suffer an estimation ambiguity error. In concrete terms, *B&B* and $F2$ share the FRA ambiguity of $k\pi/2$, and *Li*1, *Li*2, *Ch*3, *Ch*6 and $W1$ share the same ambiguity of $k\pi$, where k is an unknown integer and called the ambiguity magnitude. The FRA ambiguity can be divided into pixel-level and the holistic image-level ambiguity, which will affect the estimation performance [22].

B. EXPERIMENTS OF FR ESTIMATION

Experiments of FR estimation should be operated in order to validate the effectiveness of FR estimators. The typical L-band systems, such as the PALSAR and in-orbit ALOS-2, are applicable. A free archive of the PALSAR data is available online at https://vertex.daac.asf.alaska.edu/ and limited sample products of the ALOS-2 data are provided by the JAXA official website, whose quality is confirmed in calibration and validation. A set of PALSAR data was obtained in Chongqing on May 2007 (numbered as ALPSRP061640560), in Washington on October 2007 (numbered as ALPSRP090962830), in the Yellow River Delta of Dongying on December 2007 (numbered as ALPSRP099560750), and in the eastern sea areas beside Philippines on March 2007 (numbered as ALPSRP061780310), denoted as Data $1-4$, respectively. And a wider scene of the ALOS-2 data was obtained in the CuaDat dam of Vietnam on November 2014, which could be denoted as Data 5 (numbered as ALOS2024040390).

It is in general supposed that FRA estimates are normally distributed, and tend to be significantly influenced by system noise, and hence take on a dispersive distribution around the average value. Data 5 is selected and applied to the Pauli decomposition and shown as a pseudo image in FIGURE 3(a). Radar parameters corresponding to Data 5 are summarized in TABLE 1. The original PolSAR data is then implemented via *B&B* for instance as to each pixel, and the result is shown in FIGURE 3(b). It is indicated that the FRA estimates with a mean value of 3.8393° and an estimated accuracy of 9.0664° are imposed by a scattering distribution ranging from −45° to 45° mainly because of the considerable noise. Besides, the evident dependence on surface features emerges in the FRA estimates, which is resulted from different SNRs as to various surface features. Moreover, for river or lake regions, the FRA estimates tend to be more scattering owing

TABLE 1. Radar parameters of data 5.

Parameters	Specification	Unit
Radar frequency	1.27	GHz
Azimuth lines	23210	-
Range samples	7384	-
Azimuth pixel spacing	2.9911	m
Range pixel spacing	9.3685	m
Near range	717369.0000	m
Center range	751952.8706	m
Far range	786536.7412	m
Sar to Earth center	7009271.4888	m
Earth radius below sensor	6375829.0992	m
Center latitude	20.1040	deg
Center longitude	105.8266	deg
Incident angle	34.3838	deg

to the lower SNR in these areas. Averaging by a box car filter according to the mathematical expectation in the expressions of FR estimators is a practical method to restrict system noise [19]–[21]. FRA estimates passing through an average filter with 10×10 pixels is illustrated in FIGURE 3(c) with a mean value of 4.0946° and an estimated accuracy of 0.7518°, and the result indicates a more centralized distribution than that in FIGURE 3(b), due to the depressed system noise.

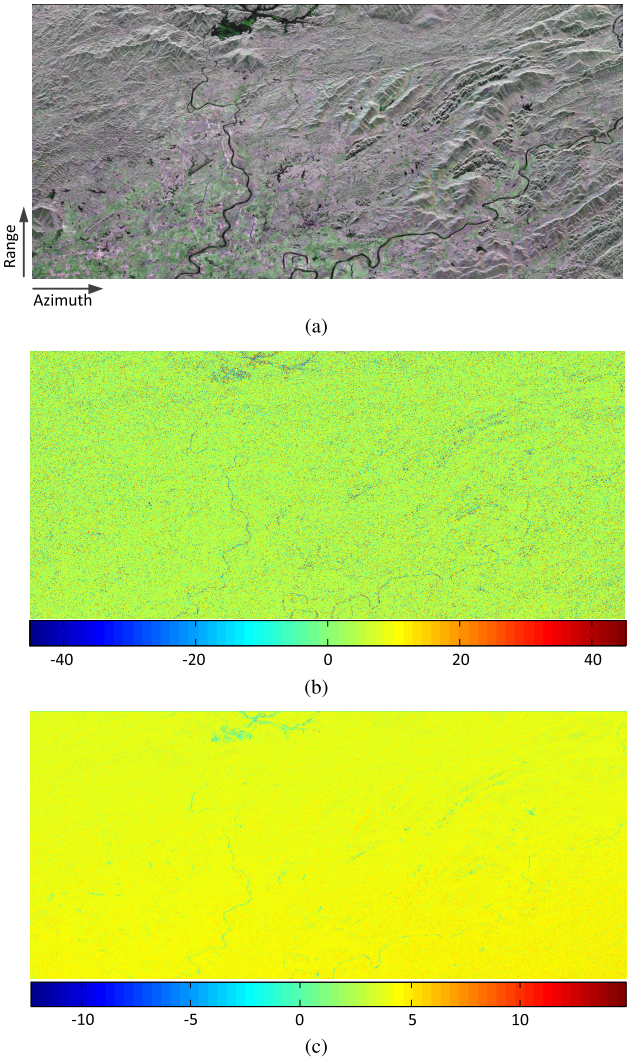

FIGURE 3. Experiments of FR estimation based on Data 5. (a) Original pseudo image (Pauli decomposition with Red = HH, Green = HV, Blue = VV). (b) Spatial distribution of FRA estimates (deg) without an average filter. (c) Spatial distribution of FRA estimates (deg) by a box car filter of 10×10 pixels.

The scattering distribution diagram is valuable for a better description, and $|Y_{23}| = |Z_{21}Z_{12}^*|$ can be regarded as the signal intensity that is relative with the signal to noise ratio (SNR) [23]. The FRA estimates in FIGURE 3(b) and FIGURE 3(c) are shown as scatter diagrams in FIGURE 4(a) and FIGURE 4(b), respectively. It is indicated that those pixels or blocks with higher SNRs tend to have FRA estimates closer to the average value. As shown in

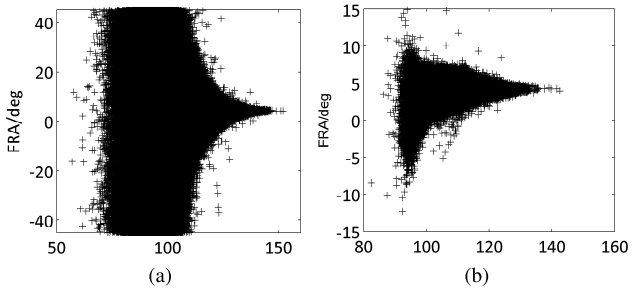

FIGURE 4. Experiments of FR estimation based on Data 1 versus $|Y_{23}|$ measured in dB. (a) Original pseudo image (Pauli decomposition). (b) A distribution of FRA estimates without an average filter.

TABLE 2. Experimental results of FR estimation based on data $1 - 5$ (Units: Degree).

	Data 1	Data 2	Data 3	Data 4	Data 5
$B\&B$	0.1199	1.9593	0.5546	0.4018	4.0946
$F2$	3.3636	4.2994	5.0506	2.0134	6.6257
$Ch3$	0.0616	1.7273	0.3635	0.3724	3.9258
$Ch6$	0.0513	1.7624	0.0918	0.3025	1.6553
$Li1$	0.0774	1.8841	0.6655	0.1965	3.4667
$Li2$	0.1164	1.9404	0.2881	0.7522	3.7189
$W1$	0.1318	1.8814	0.2406	0.3924	4.1400

FIGURE 4(b), an approximately normal distribution of FRA estimates are more concentrated due to the use of a box car filter. Without special declaration, all following experiments of FR estimation will be performed by utilizing a box car filter with a 10×10 window, according to the mathematical expectation in the corresponding expressions of relevant FR estimators.

FR estimation with an average filter is operated by utilizing Data $1 - 5$ and results of the average values are summarized in TABLE 2. It can be observed that the FRA estimates of the respective estimators are close with each other, other than $F2$, which seems to be a distinctive and unqualified one, with the FRA estimates much larger than the others. Furthermore, all summarized FRA estimates are lower than 10°. It is mainly due to the fact that both two satellites ran in sun-synchronous orbits and acquired raw data at the local time of night, when the TEC was in a low condition. By the way, the two satellites experienced a minimum of the ionospheric activity in the 11-years solar cycle [23].

C. THEORETICAL ANALYSIS OF ESTIMATION PERFORMANCE

At first, it should be noted that the backscatter reciprocity and azimuth reflection symmetry principles are both conditioned in $Li1$, $Li2$ and $W1$, while $B\&B$, $F2$, $Ch3$, $Ch6$ are merely in premise of the backscatter reciprocity. As polarimetric measurements within a SAR image are not uniformly oriented in azimuth direction, that is only satisfied for simple scattering models [14], [15], the hypothesis of so-called reflection symmetry is not ideally tenable. As a result, $Li1$, $Li2$ and $W1$ may not be robust as to the complex scattering type.

Besides the above-mentioned published estimators, potential combination of the items in (36) and (38) can obtain new FR estimators, for example

$$\Omega_1 = \frac{1}{2}\tan^{-1}\left[\frac{Re\,(Y_{12}-Y_{13})}{Im\,(Y_{12}+Y_{13})}\right], \tag{31}$$

$$\Omega_2 = \frac{1}{2}\tan^{-1}\left[\frac{Re\,(Y_{34}-Y_{24})}{Im\,(Y_{34}+Y_{24})}\right], \tag{32}$$

and so on. We have also made some efforts to look for a novel estimator with the optimal robustness, like the jobs made in [18]–[21], but it fails. In fact, tens of potential new estimators can be derived from the linear or circular PCM, nevertheless it is intractable to operate performance analysis for so many estimators to select the optimal one.

No matter what is the item combination to produce new estimators, the signal amplitude can be an alternative principle to evaluate estimation performance as to the signal to noise ratio (SNR) in theory. In detail, the signal amplitude of (38h) in *B&B* is $\{O_{11}+O_{44}+2Re\,(O_{14})\} = |S_{hh}+S_{vv}|^2$; that in $F2$ is $|S_{hh}+S_{vv}|$; the combination magnitude in $Ch3$ and $Ch6$ is $Im\,(O_{14})$ and $Im\,(O_{12}-O_{24})$, respectively; that in $Li1$ and $Li2$ is $(O_{11}-O_{44})$ and $Re\,(O_{12}+O_{13}+O_{24}+O_{34})$ respectively; that in $W1$ is $(O_{11}-O_{44})$; that in (31) and (32) is $(O_{11}-O_{44})$. For $Ch6$ and $Li2$, its combination magnitude is a function of the reflection symmetric items, that is close to zero despite the non-ideal assumption [14]. It shows the low SNR for FR estimation of $Ch6$ and $Li2$. In addition, the signal amplitude of $Li1$, $W1$ and the two new estimators is related to the differential intensity of the HH and VV channels. To sum up, the signal amplitude in the earliest estimator is the largest one in theory; *B&B* is bound to have the optimal robustness, which will be verified in next analysis.

D. PERFORMANCE ANALYSIS OF FR ESTIMATORS

1) SENSITIVITY TO OTHER POLARIMETRIC DISTORTIONS

According to (15), the measured scattering matrix is influenced by other polarimetric distortions in addition to FR, e.g., system noise, channel imbalance and crosstalk [18]–[21]. As a result, it is necessary to assess the impacts of these system perturbations on FR estimators. Then, experiments should be implemented by adding these element to a data without FR effects. A pure real data can be obtained after the symmetrization operation on the original data, which is easily expressed as $M_{hv}^{sym} = M_{vh}^{sym} = (M_{hv}+M_{vh})/2$. Furthermore, the signal to noise ratio (SNR) for a full polarimetric SAR data is defined as

$$SNR = \frac{\langle S_{hh}S_{hh}^*\rangle + 2\langle S_{hv}S_{hv}^*\rangle + \langle S_{vv}S_{vv}^*\rangle}{\langle N_{hh}N_{hh}^*\rangle + 2\langle N_{hv}N_{hv}^*\rangle + \langle N_{vv}N_{vv}^*\rangle}, \tag{33}$$

and the SNR is artificially varying from 0 dB to 20 dB in following experiments. In addition, as a matter of convenience for experiments, perturbations between different channels are assumed to be constant as

$$\begin{aligned} f_0 &= f_1 = f_2, \\ \delta_0 &= \delta_1 = \delta_2 = \delta_3 = \delta_4, \\ \langle N_{hh}N_{hh}^*\rangle &= \langle N_{hv}N_{hv}^*\rangle = \langle N_{vh}N_{vh}^*\rangle = \langle N_{vv}N_{vv}^*\rangle. \end{aligned} \tag{34}$$

The amplitude and phase parameters of f_0 can be set to vary from 0 dB to 1 dB and 0° to 10°, respectively, and the channel crosstalk δ_0 is set to have a range from −40 dB to −10 dB. A true FRA value of 10° is injected into Data 1, whose original FRA has been eliminated with the preliminary application of the symmetrization operation. The RMS principle employed in the existent researches tends to confuse the estimation bias with STD [19], [20]. Therefore, rather than RMS, both of the estimation bias and STD versus SNR, f_0 and δ_0 are illustrated for a comprehensive evaluation, and results are described in FIGURE 5.

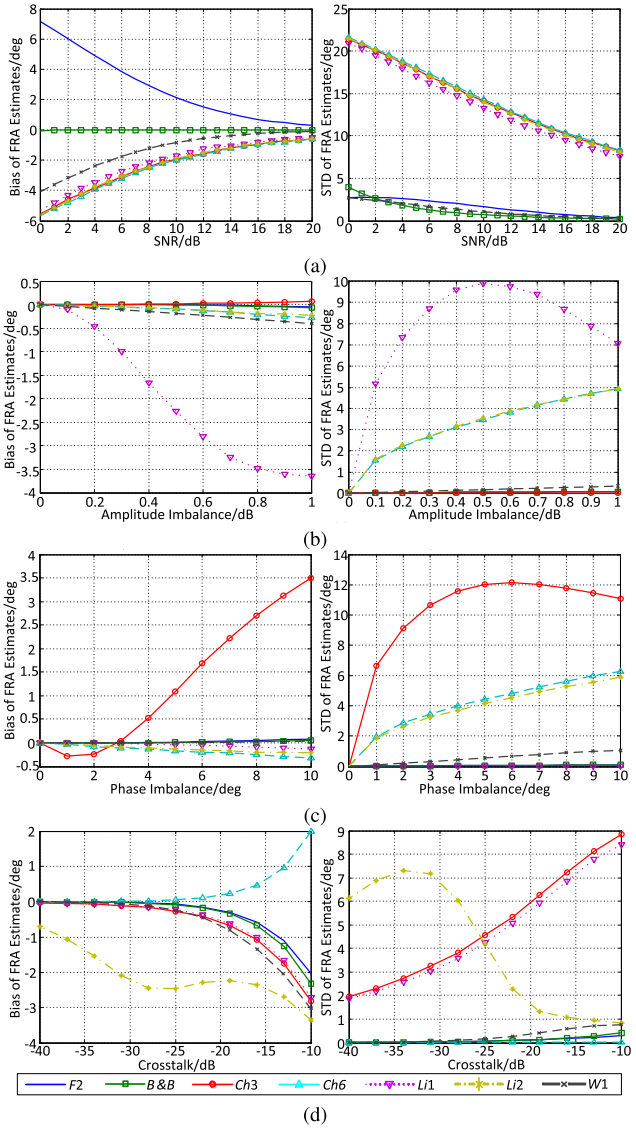

FIGURE 5. Sensitivity evaluation of FR estimators shown as estimation bias and standard deviation. (a) SNR. (b) Amplitude imbalance. (c) Phase imbalance. (d) Channel crosstalk.

As to SNR, it is shown in FIGURE 5(a) that *B&B* has the superior robustness and $W1$ takes second place. Furthermore, other estimators, including $F2$, $Li1$, $Li2$, $Ch3$ and $Ch6$ seem to be incompetent, for a reason that $F2$ has a larger estimation biases despite the low standard deviations; $Li1$, $Li2$, $Ch3$ and $Ch6$ share a closely consistent and intensive sensitivity. As to the channel imbalance, including the amplitude imbalance shown in FIGURE5(b) and the phase imbalance described in FIGURE 5(c), *B&B* and $F2$ share the optimal performance. Although $Ch3$ also shows the optimal performance regarding the amplitude imbalance, it performs poorly in terms of the phase imbalance; the condition is inverse for $Li1$. Finally, as to the channel crosstalk shown in FIGURE 5(d), $Ch6$ shows the optimal performance, while *B&B* and $F2$ share the nearly consistent robustness.

2) SENSITIVITY TO TRUE FRA

Some studies also mentioned that the performance of FR estimation could be dependent on the true value of FRA [19]–[21]. Hence, relevant experiments on basis of Data 1 are implemented with a typical calibrated system ($SNR = 20dB$, $|f_0| = 0.5dB$, $arg\,(f_0) = 1deg$, $|\delta_0| = -25dB$), and the result is shown in FIGURE 6. It is concluded that $F2$ is least sensitive, but it has been abandoned for its bad performance in terms of SNR. *B&B* also shows good robustness to the true FRAs. In addition, all estimators tend to become deteriorated when the true of FRA is close to 45°. It is mainly resulted from the ambiguity inconsistency of the FRA estimates within a SAR image [25].

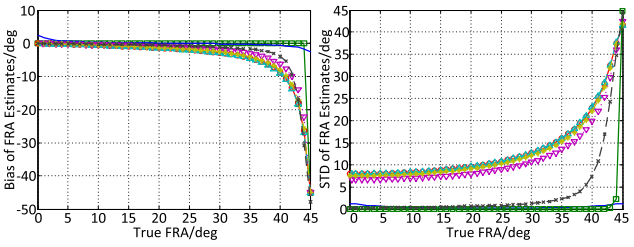

FIGURE 6. Sensitivity of FR estimators to true FRA shown as estimation bias and standard deviation.

To conclude, *B&B* proves to be the optimal one. On the whole, it shows the best robustness as to system noise, channel imbalance, crosstalk and the true FRA. Other estimators are eliminated because of one particular aspect or more with bad performance, mainly in virtue of their strong dependence upon the reflection symmetry principle or SNR weakness in their mathematic expressions. Hence, *B&B* with the optimal robustness will be applied to the following FRA map.

V. RETRIEVAL OF THE SPATIAL-VARIABLE FRA DISTRIBUTION

A. AN FRA MAP PROCEDURE

As mentioned above, it is likely that the FRAs within a SAR image tend to have a spatial-variable distribution, mainly due to the medium-scale background ionosphere and the visible range with a variation from the close to far swath. A step-to-step procedure for mapping the spatial FRAs is proposed and illustrated in FIGURE 7, which is described as follows.

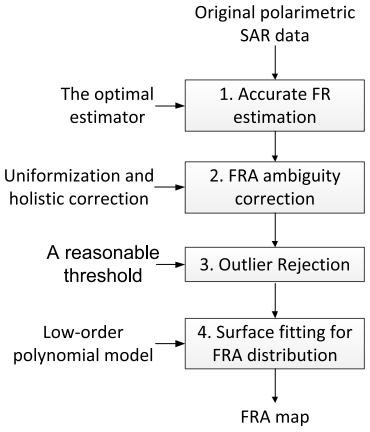

FIGURE 7. A step-to-step procedure for the FRA map.

In the first place, accurate FR estimation are necessary for the FRA map, and thus the optimal estimator is applied. It is necessary to depress the system noise to obtain a centralized distribution of FRAs. As mentioned above, we can use a box car filter with a typical window size; its estimation accuracy will be improved by enlarging the window size of the average filter, which nevertheless tends to blur the spatial structures of the FRA distribution at the same time.

In the second place, the FRA ambiguity correction, including the ambiguity uniformization and the holistic ambiguity correction, is unnecessary for the L-band missions, but it may be demanded for the future P-band missions to get accurate FRA estimates [22]. The ambiguity uniformization should be particularly solved. When the wrapped FRA is close to ±45°, the ambiguity magnitude is not consistent, and the estimates are classified into two groups: one close to 45° and the other close to −45°. Total numbers of the two groups are counted and represented as K1 and K2, respectively. According to the maximal likelihood principle, the group with the quantitative superiority is more likely to occur, and the magnitude of the other group should be modified. For example, if K_1 is larger than K_2, the FRA estimates close to −45° should add 90°; otherwise, the estimates close to 45° should be subtracted by 90°. At last, the holistic ambiguity correction can be solved by using FR prediction [19].

Thirdly, a reasonable range of the FRA fluctuation should be selected as a criterion to eliminate estimation anomalies from the estimation results. Generally, the FRA estimates can be considered as the fluctuations corresponding to the global estimation result, and it is known that FRA fluctuations are relatively slight within a real SAR image [8]. Hence, if some estimated results surpass the reasonable range, those pixels or blocks should be masked and eliminated as bad estimates. Given that the FRA estimates approximate a normal distribution, $\mu \pm n\xi$ (μ is the average, ξ is the standard diviation and n is an unknown integer) can be be used as a reference

range and the confidence probability can respectively reach 68.27 %, 95.45 %, 99.74 % for $n = 1, 2, 3$. The confidence probability is important for the FRA map, which can be artificially determined by predicted range of FRAs based on the local predicted ionospheric status, the carrier frequency and the scene size of the PolSAR data. Furthermore, the another criterion should also be as a reference of the outlier rejection that the FRA value is positive in the northern hemisphere and negative in the southern hemisphere [13]. Based on these criteria, the mask can be generated and untrustful results can be effectively eliminated.

At last, it is supposed that the selected pixels or blocks are trustful and can be used in the surface fitting procedure. The objective of the surface fitting is to provide the FRA map for the holistic scene. In virtue of the slow variation of FRAs, only linear and quadratic components are sizable and need to be considered. Therefore, a simple surface fitting approach is based on a 2-order and 2-dimensional polynomial model, and can be given as

$$\Omega(x, y) = \Omega_0 + c_1 x + c_2 y + c_3 x^2 + c_4 y^2 + c_5 xy \quad (35)$$

where Ω_0 is the constant FRA value which can be considered as the holistic part of the FRA distribution, c_1, c_2 represent the linearly variable coefficients, c_3, c_4 stand for the quadratically variable coefficients, and c_5 indicates the coupling coefficient. The obtained FRA map can be employed to calibrate polarimetric distortions and further derive the ionospheric TEC map, which can be adopted to correct other ionospheric effect for the spaceborne PolSAR image.

B. SIMULATION VALIDATION OF THE FRA MAP BY USING AIRBORNE P-BAND POLSAR DATA

In an attempt to explore the feasibility of retrieving a spatial distribution of FRAs from spaceborne PolSAR data, a set of airborne P-band PolSAR image data is employed, which was obtained in $35.53°N, 110.49°E$ on 29th December 2015. In following simulations, the SAR payload is artificially moved to the PALSAR's orbit, a sun-synchronous orbit at the height of 695 kilometers. Its system parameters are summarized in TABLE 3. Due to the unknown polarimetric calibration quality, the original PolSAR data is processed by symmetrization, and a typical calibration of $SNR = 20dB$, $|f_0| = 0.5dB$, $arg(f_0) = 1deg$, $|\delta_0| = -25dB$ is injected into the pure data. The local VTEC value at midday of that day is predicted by utilizing the IRI and estimated as a crude reference of 20.7 TECU. It is converted to STEC with 33.9 TECU on basis of the satellite-to-earth geometric relationship. Furthermore, the TEC-to-FRA coefficient is predicted to be 1.35 deg/TECU by adopting the IGRF; thus the predicted FRA is 45.8 degrees. A spatial FRA distribution nearly varying 44.3° to 47.9° is simulated and illustrated in FIGURE 8. It is injected into the pure image, and the Pauli decomposition of the original and contaminated images is shown in FIGURE 9. In comparison, it shows that the original polarimetric characteristic has been seriously distorted by FR impacts, which should be estimated and corrected.

TABLE 3. System parameters of the airborne P-band PolSAR data.

Parameters	Specification	Unit
Radar frequency	600	MHz
Radar Bandwidth	200	MHz
Azimuth lines	8000	-
Range samples	4000	-
Azimuth pixel spacing	0.612882	m
Range pixel spacing	0.625000	m
Center latitude	35.53	deg
Center longitude	110.49	deg
Look-down angle	52.3849	deg

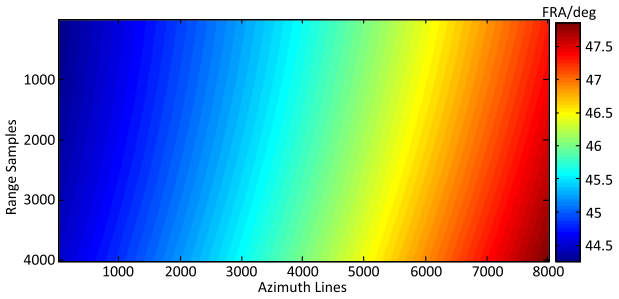

FIGURE 8. Simulated spatial distribution of FRAs.

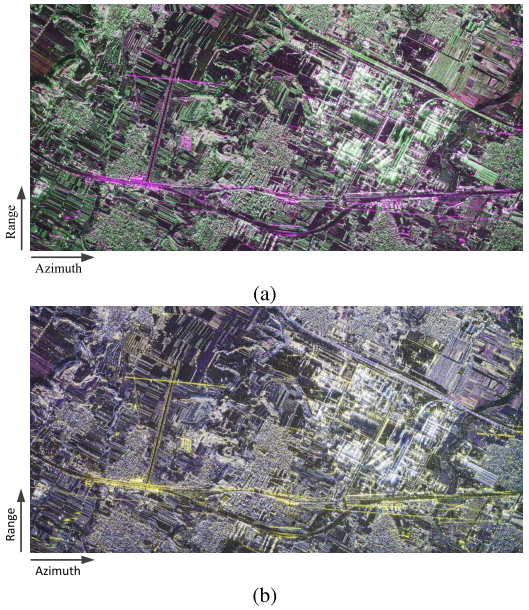

FIGURE 9. Simulation of effects of spatial FRAs on airborne P-band PolSAR data. (a) Pure image (Pauli decomposition with Red = HH, Green = HV, Blue = VV). (b) Contaminated PolSAR image by spatial FRAs.

Therefore, the *B&B* estimator as the optimal one is adopted to estimate FRAs. An averaging filter with a window size of 30×30 is utilized to obtain a more centralized distribution of FRAs. The FR estimation result is described as a scattering distribution diagram in FIGURE 10(a). It shows that the FRA distribution is split into two groups, one group close to 45°

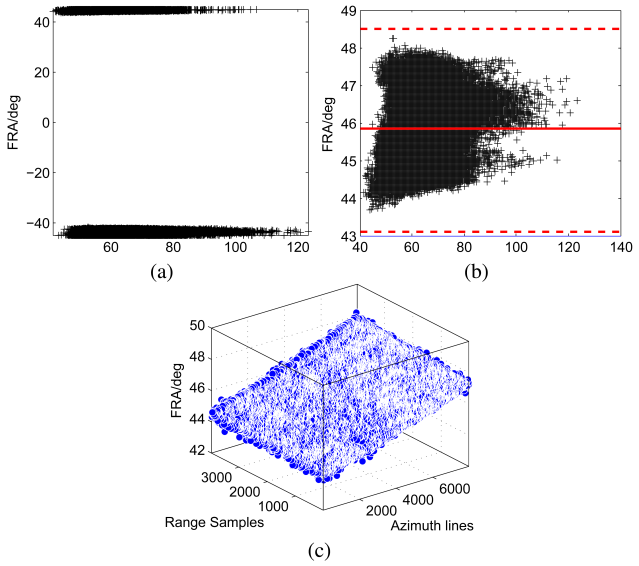

FIGURE 10. FRA mapping processing for the contaminated P-band PolSAR image. (a) Scattering distribution diagram versus $|Y_{23}|$ measured in dB for FR estimation. (b) Scattering distribution diagram after removing FRA ambiguity errors. (c) Surface fitting processing.

and another group close to $-45°$, which means the ambiguity magnitude is not uniform and demands for rectification. After performing the ambiguity unification and holistic correction, the scattering distribution diagram is modified and illustrated in FIGURE 10(b). The average FRA value is 45.8° and the estimation STD is 0.90°. The trustful interval within $\mu \pm 3\xi$ is employed, due to the known variable range of FRAs in our simulation; of course, this range is generally sheltered in real data processing, but it can be predicted with an application of external database. Based on the outlier rejection, the trustful interval derived from the average and STD is from 43.1° to 48.5° degrees and illustrated as red dashed lines in FIGURE 10(b). All FRA estimates are within the trustful interval and thus remain to be employed in surface fitting, which is shown in FIGURE 10(c). Finally, the differential map derived from the original and retrieved FRA maps is illustrated in FIGURE 11(a), which is based on FR estimation by employing *B&B*. Eventual FRA biases are tiny components, less than 5×10^{-3} degrees, which validates the effectiveness of the FRA map.

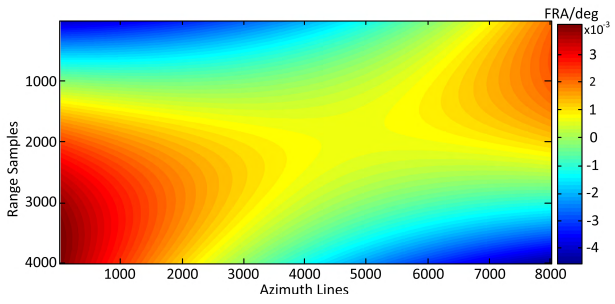

FIGURE 11. Differential FRA maps in contrast to the original distribution.

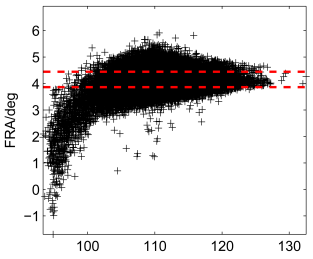

FIGURE 12. Accurate FRA estimates for Data 5 are shown as scattering distribution diagrams versus $|Y_{23}|$ measured in dB.

C. A REAL DATA PROCESSING EXAMPLE BASED ON ALOS-2 POLSAR DATA

1) THE FRA MAP

The processing here is based on ALOS-2 data because of its wider swath than PALSAR, which shows more potential to contain varying FRA terms. As depicted in FIGURE 3, FR estimation has been implemented for Data 5, but the FRA estimates are still distributed in a wide variation even with a 10×10 averaging filter. For the L-band mission with a similar scene size to the Data 5, the spatial variation of FRAs is predicted not to surpass 1°. Therefore, in the FRA mapping procedure, an averaging filter with a larger window of 50×50 and the $\mu \pm \xi$ principle of outlier rejection should be applied to the *B&B*, which is suitable to preserve the spatial structure of FRAs. A scattering distribution diagram is shown in FIGURE 12 with a mean value of 4.1536° and an accuracy of 0.2906°. According to the outlier rejection that sifts those estimates out of $\mu \pm \xi$, a reasonable interval calculated from the average and STD is also illustrated as red dashed lines in FIGURE 12. Even though the FRA estimates do not strictly obey normal distribution, those selected pixels or blocks are still more than a half, which is considered to be reasonable. The ambiguity correction is not required for this case. Then, these trustful estimates are applied to the surface fitting, and the FRA map is described in FIGURE 13. It indicates that the significant trend of the FRA variation emerges in the range direction, which is mainly due to the STEC varying from the close to far swath.

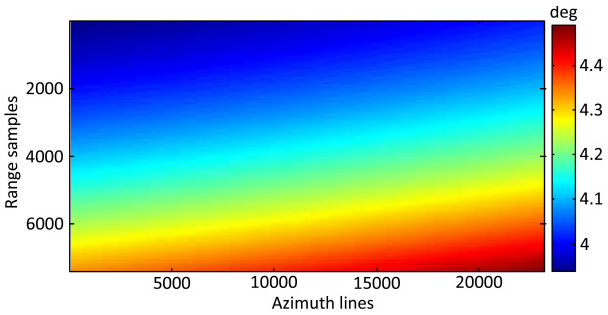

FIGURE 13. Experimental result of the FRA map for Data 5.

2) FURTHER DERIVATION FOR THE IONOSPHERIC MAP

According to (20), we can further calculate the ionospheric STEC and VTEC maps from the FRA map. On basis of the geographic location and radar parameters that is summarized in TABLE 1, the TEC-to-FRA coefficient of Data 5 can be derived via IGRF, which is approximately 0.1234 deg/TECU. Hence, we further illustrate the STEC map in FIGURE 14(a). The spatial distribution of $\sec\chi\,(x, y)$ can be modeled as $R\,(x, y)\,/H_s$, where H_s is the satellite altitude, and $R\,(x, y)$ represents the slant range of each pixel within the image and approximates a linear variation from the close to far swath. By calculating $\sec\chi\,(x, y)$, the VTEC map is further derived and described in FIGURE 13(b). The result indicates that the ionospheric map is an alternative method for ionospheric sounding, which is beneficial to mitigating background ionospheric effects for PolSAR data.

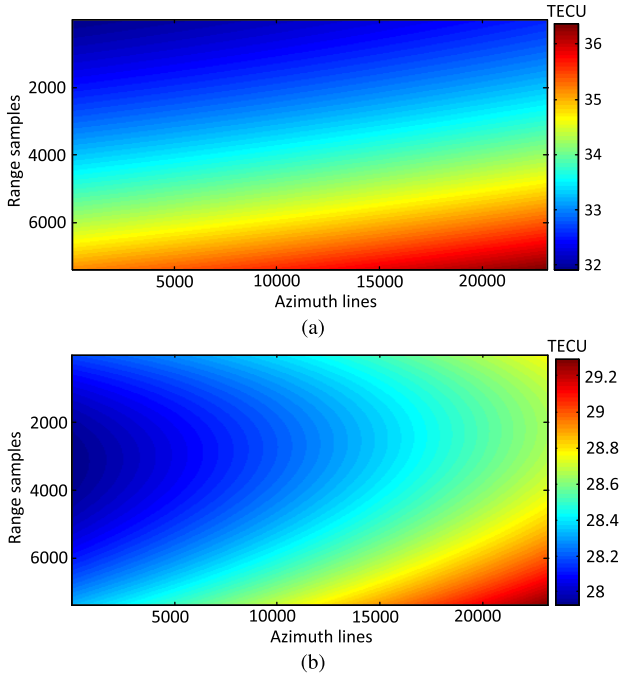

FIGURE 14. The maps of the background ionosphere. (a) The STEC map. (b) The VTEC map.

VI. CONCLUSION

The FR impact is a significant distortion for the polarimetric application of the spaceborne SAR system, which operates at L-band or P-band. Mainly caused by background ionosphere, the FRA values within a SAR image have a potential spatial-variable distribution, which is particularly investigated in this paper. Even though there are still novel FR estimators we can derive, theoretical analysis of estimation performance shows the earlist one has the optimal robustness. This mathematical conclusion is validated by performing comprehensive performance analysis. At last, an improved step-to-step procedure with consideration of the potential FRA ambiguity inconsistency is proposed and realized via simulation. The real data processing based on ALOS-2 data demonstrates the potential of the FRA or ionospheric TEC map. In the near future, more PolSAR data obtained by both L-band and P-band missions are available with high quality. We expect to further validate the effectiveness of the FRA map. Based on the FRA map, an alternative approach of ionospheric sounding or tomography comes true, and the ionospheric impacts on original images and subsequent applications can be effectively compensated.

APPENDIX
LINEAR OR CIRCULAR PCM

The covariance matrix of (22) can be expressed as $C_{ik} = \langle M_i M_k^* \rangle$, where $\langle\cdot\rangle$ means the mathematic expectation, i and k take the value of 1, 2, 3, 4, and it has $[M_1,\ M_2,\ M_3,\ M_4] = [M_{hh},\ M_{hv},\ M_{vh},\ M_{vv}]$. Therefore, each item of the linear PCM can be expanded as

$$\begin{aligned}
C_{11} &= O_{11}\cos^4\Omega + O_{44}\sin^4\Omega \\
&\quad - 2Re\,(O_{14})\sin^2\Omega\cos^2\Omega, && (36a)\\
Re\,(C_{12}) &= Re\,(O_{12})\cos^2\Omega - Re\,(O_{24})\sin^2\Omega \\
&\quad - O_{11}\sin\Omega\cos^3\Omega + O_{44}\sin^3\Omega\cos\Omega \\
&\quad - \frac{1}{4}Re\,(O_{14})\sin\ 4\Omega, && (36b)\\
Im\,(C_{12}) &= Im\,(O_{12})\cos^2\Omega + Im\,(O_{24})\sin^2\Omega \\
&\quad - \frac{1}{2}Im\,(O_{14})\sin\ 2\Omega, && (36c)\\
Re\,(C_{13}) &= Re\,(O_{12})\cos^2\Omega - Re\,(O_{24})\sin^2\Omega \\
&\quad + O_{11}\sin\Omega\cos^3\Omega - O_{44}\sin^3\Omega\cos\Omega \\
&\quad + \frac{1}{4}Re\,(O_{14})\sin\ 4\Omega, && (36d)\\
Im\,(C_{13}) &= Im\,(O_{12})\cos^2\Omega + Im\,(O_{24})\sin^2\Omega \\
&\quad + \frac{1}{2}Im\,(O_{14})\sin\ 2\Omega, && (36e)\\
C_{14} &= -(O_{11} + O_{44})\sin^2\Omega\cos^2\Omega + Re\,(O_{14}) \\
&\quad \times \left(\sin^4\Omega + \cos^4\Omega\right) + jIm\,(O_{14})\cos 2\Omega, && (36f)\\
C_{22} &= O_{22} + [O_{11} + O_{44} + 2Re\,(O_{14})]\sin^2\Omega\cos^2\Omega \\
&\quad - Re\,(O_{12} + O_{24})\sin\ 2\Omega, && (36g)\\
C_{23} &= O_{22} - [O_{11} + O_{44} + 2Re\,(O_{14})]\sin^2\Omega\cos^2\Omega \\
&\quad - jIm\,(O_{12} - O_{24})\sin\ 2\Omega, && (36h)\\
Re\,(C_{24}) &= -Re\,(O_{12})\sin^2\Omega + Re\,(O_{24})\cos^2\Omega \\
&\quad + O_{11}\sin^3\Omega\cos\Omega - O_{44}\sin\Omega\cos^3\Omega \\
&\quad - \frac{1}{4}Re\,(O_{14})\sin\ 4\Omega, && (36i)\\
Im\,(C_{24}) &= Im\,(O_{12})\sin^2\Omega + Im\,(O_{24})\cos^2\Omega \\
&\quad - \frac{1}{2}Im\,(O_{14})\sin\ 2\Omega, && (36j)\\
Re\,(C_{34}) &= -Re\,(O_{12})\sin^2\Omega + Re\,(O_{24})\cos^2\Omega \\
&\quad - O_{11}\sin^3\Omega\cos\Omega \\
&\quad + O_{44}\sin\Omega\cos^3\Omega + \frac{1}{4}Re\,(O_{14})\sin\ 4\Omega, && (36k)
\end{aligned}$$

$$Im(C_{34}) = Im(O_{12})\sin^2\Omega + Im(O_{24})\cos^2\Omega + \frac{1}{2}Im(O_{14})\sin 2\Omega, \quad (36l)$$

$$C_{33} = O_{22} + [O_{11} + O_{44} + 2Re(O_{14})]\sin^2\Omega\cos^2\Omega + Re(O_{12} + O_{24})\sin 2\Omega, \quad (36m)$$

$$C_{44} = O_{11}\sin^4\Omega + O_{44}\cos^4\Omega - 2Re(O_{14})\sin^2\Omega\cos^2\Omega, \quad (36n)$$

$$C_{21} = C_{12}^*, \quad C_{31} = C_{13}^*, \quad C_{32} = C_{33}^*, \quad C_{41} = C_{14}^*, \quad C_{42} = C_{42}^*, \quad C_{43} = C_{43}^*, \quad (36o)$$

where $Re(\cdot)$ and $Im(\cdot)$ takes the real and imaginary parts of a complex, respectively. $O_{ik} = \langle S_i S_k^* \rangle$, where i and k take the value of 1, 2, 3, 4, and $[S_1, S_2, S_3, S_4] = [S_{hh}, S_{hv}, S_{vh}, S_{vv}]$ with $S_2 = S_3$. From a viewpoint of the information content of polarimetric measurements, the measured linear-polarized matrix in (21) is equivalent to the circular-polarized basis, which can be derived from

$$\begin{bmatrix} Z_{hh} & Z_{vh} \\ Z_{hv} & Z_{vv} \end{bmatrix} = \begin{bmatrix} 1 & j \\ j & 1 \end{bmatrix} \begin{bmatrix} M_{hh} & M_{vh} \\ M_{hv} & M_{vv} \end{bmatrix} \begin{bmatrix} 1 & j \\ j & 1 \end{bmatrix}. \quad (37)$$

Hence, the PCM of the circularly polarized basis can be expressed as $Y_{ik} = \langle Z_i Z_k^* \rangle$, where i and k take the value of 1, 2, 3, 4, and it has $[Z_1, Z_2, Z_3, Z_4] = [Z_{hh}, Z_{hv}, Z_{vh}, Z_{vv}]$. Each element of the circular PCM can be expanded and expressed as

$$Y_{11} = O_{11} + O_{44} - 2Re(O_{14}) + 4O_{22} + 4Im(O_{12} + O_{24}), \quad (38a)$$

$$Re(Y_{12}) = 2Re(O_{12} + O_{24})\cos 2\Omega + 2Im(O_{24} - O_{12}) \times \sin 2\Omega - (O_{11} - O_{44})\sin 2\Omega + 2Im(O_{14}) \times \cos 2\Omega, \quad (38b)$$

$$Im(Y_{12}) = -2Re(O_{12} + O_{24})\sin 2\Omega + 2Im(O_{24} - O_{12}) \times \cos 2\Omega - (O_{11} - O_{44})\cos 2\Omega - 2Im(O_{14}) \times \sin 2\Omega, \quad (38c)$$

$$Re(Y_{13}) = 2Re(O_{12} + O_{24})\cos 2\Omega - 2Im(O_{24} - O_{12}) \times \sin 2\Omega + (O_{11} - O_{44})\sin 2\Omega + 2Im(O_{14}) \times \cos 2\Omega, \quad (38d)$$

$$Im(Y_{13}) = 2Re(O_{12} + O_{24})\sin 2\Omega + 2Im(O_{24} - O_{12}) \times \cos 2\Omega - (O_{11} - O_{44})\cos 2\Omega + 2Im(O_{14}) \times \sin 2\Omega, \quad (38e)$$

$$Y_{14} = -O_{11} - O_{44} + 2Re(O_{14}) + 4O_{22} + 4jRe(-O_{12} + O_{24}), \quad (38f)$$

$$Y_{21} = Y_{12}^*, \quad Y_{22} = O_{11} + O_{44} + 2Re(O_{14}), \quad (38g)$$

$$Y_{23} = \{O_{11} + O_{44} + 2Re(O_{14})\}\exp\{j4\Omega\}, \quad (38h)$$

$$Re(Y_{24}) = 2Re(O_{12} + O_{24})\cos 2\Omega - 2Im(O_{12} - O_{24}) \times \sin 2\Omega + (O_{11} - O_{44})\sin 2\Omega + 2Im(O_{14}) \times \cos 2\Omega, \quad (38i)$$

$$Im(Y_{24}) = 2Re(O_{12} + O_{24})\sin 2\Omega + 2Im(O_{12} - O_{24}) \times \cos 2\Omega - (O_{11} - O_{44})\cos 2\Omega + 2Im(O_{14}) \times \sin 2\Omega, \quad (38j)$$

$$Re(Y_{34}) = 2Re(O_{12} + O_{24})\cos 2\Omega + 2Im(O_{12} - O_{24}) \times \sin 2\Omega - (O_{11} - O_{44})\sin 2\Omega + 2Im(O_{14}) \times \cos 2\Omega, \quad (38k)$$

$$Im(Y_{34}) = -2Re(O_{12} + O_{24})\sin 2\Omega + 2Im(O_{12} - O_{24}) \times \cos 2\Omega - (O_{11} - O_{44})\cos 2\Omega - 2Im(O_{14}) \times \sin 2\Omega, \quad (38l)$$

$$Y_{31} = Y_{13}^*, \quad Y_{32} = Y_{23}^*, \quad Y_{33} = Y_{22}, \quad (38m)$$

$$Y_{41} = Y_{14}^*, \quad Y_{42} = Y_{24}^*, \quad Y_{43} = Y_{34}^*, \quad (38n)$$

$$Y_{44} = O_{11} + O_{44} - 2Re(O_{14}) + 4O_{22} - 4Im(O_{12} + O_{24}). \quad (38o)$$

ACKNOWLEDGEMENT

The authors would like to appreciate the ALOS and ALOS-2 teams of the JAXA for providing free spaceborne L-band SAR data with high quality. They are also grateful to No. 38th institute of the China Electronics Technology Group Corporation for providing airborne P-band PolSAR data.

REFERENCES

[1] D. L. Knepp and H. L. F. Houpis, "ALTAIR VHF/UHF observations of multipath and backscatter enhancement," *IEEE Trans. Antennas Propag.*, vol. 39, no. 4, pp. 528–534, Apr. 1991.
[2] E. Rignot, R. Zimmermann, J. van Zyl, and R. Oren, "Spaceborne applications of a P-band imaging radar for mapping of forest biomass," *IEEE Trans. Geosci. Remote Sens.*, vol. 33, no. 5, pp. 1162–1169, Sep. 1995.
[3] M. Moghaddam, S. Saatchi, and R. H. Cuenca, "Estimating subcanopy soil moisture with radar," *J. Geophys. Res.*, vol. 105, no. D11, pp. 14899–14911, Jun. 2000.
[4] M. Shimada, O. Isoguchi, T. Tadono, and K. Isono, "PALSAR radiometric and geometric calibration," *IEEE Trans. Geosci. Remote Sens.*, vol. 47, no. 12, pp. 3915–3932, Dec. 2009.
[5] K. Papathanassiou and J. S. Kim, "Pol-InSAR calibration of ALOS-2: Analysis and results from the CAL-VAL phase," in *Proc. IGARSS*, Beijing, China, Jul. 2016, pp. 3853–3854.
[6] A. Ishimaru, Y. Kuga, J. Liu, Y. J. Kim, and T. Freeman, "Ionospheric effects on synthetic aperture radar at 100 MHz to 2 GHz," *Radio Sci.*, vol. 34, no. 1, pp. 257–268, Jan. 1999.
[7] Z. W. Xu, J. Wu, and Z. S. Wu, "A survey of ionosphere effects on space-based radar," *Waves Random Media*, vol. 14, no. 2, pp. 189–273, Apr. 2004.
[8] C. Wang, M. Zhang, Z.-W. Xu, C. Chun, and D.-S. Sheng, "Effects of anisotropic ionospheric irregularities on space-borne SAR imaging," *IEEE Trans. Antennas Propag.*, vol. 62, no. 9, pp. 4664–4673, Sep. 2014.
[9] F. Meyer, R. Bamler, N. Jakowski, and T. Fritz, "The potential of low-frequency SAR systems for mapping ionospheric TEC distributions," *IEEE Geosci. Remote Sens. Lett.*, vol. 3, no. 4, pp. 560–564, Oct. 2006.
[10] Y. F. Ji, Q. L. Zhang, Y. S. Zhang, and Z. Dong, "Analysis of background ionospheric effects on geosynchronous SAR imaging," *Radioengineering*, vol. 26, no. 1, pp. 130–138, Apr. 2017.
[11] S. H. Bickel and R. H. T. Bates, "Effects of magneto-ionic propagation on the polarization scattering matrix," *Proc. IEEE*, vol. 53, no. 8, pp. 1089–1091, Aug. 1965.
[12] W. B. Gail, "Effect of Faraday rotation on polarimetric SAR," *IEEE Trans. Aerosp. Electron. Syst.*, vol. 34, no. 1, pp. 301–308, Jan. 1998.
[13] P. A. Wright, "Faraday rotation effects on L-band spaceborne SAR data," *IEEE Trans. Geosci. Remote Sens.*, vol. 41, no. 12, pp. 2735–2744, Dec. 2003.
[14] A. Freeman and S. S. Saatchi, "On the detection of Faraday rotation in linearly polarized L-band SAR backscatter signatures," *IEEE Trans. Geosci. Remote Sens.*, vol. 42, no. 8, pp. 1607–1616, Aug. 2004.
[15] R. Y. Qi and Y. Q. Jin, "Analysis of the effects of Faraday rotation on spaceborne polarimetric SAR observations at P-band," *IEEE Trans. Geosci. Remote Sens.*, vol. 45, no. 5, pp. 1115–1122, May 2007.
[16] N. C. Rogers and S. Quegan, "The accuracy of Faraday rotation estimation in satellite synthetic aperture radar images," *IEEE Trans. Geosci. Remote Sens.*, vol. 52, no. 8, pp. 4799–4807, Aug. 2014.

[17] L. Li, Y. S. Zhang, Z. Dong, and D. Liang, "Ionospheric polarimetric dispersion effect on low-frequency spaceborne SAR imaging," *IEEE Geosci. Remote Sens. Lett.*, vol. 11, no. 12, pp. 2163–2167, Dec. 2014.
[18] A. Freeman, "Calibration of linearly polarized polarimetric SAR data subject to Faraday rotation," *IEEE Trans. Geosci. Remote Sens.*, vol. 42, no. 8, pp. 1617–1624, Aug. 2004.
[19] J. Chen and S. Quegan, "Improved estimators of Faraday rotation in spaceborne polarimetric SAR data," *IEEE Geosci. Remote Sens. Lett.*, vol. 7, no. 4, pp. 846–850, Oct. 2010.
[20] L. Li, Y. S. Zhang, Z. Dong, and D. N. Liang, "New Faraday rotation estimators based on polarimetric covariance matrix," *IEEE Geosci. Remote Sens. Lett.*, vol. 11, no. 1, pp. 846–850, Jan. 2014.
[21] C. Wang, L. Liu, L. Chen, J. Feng, and H. S. Zhao, "Improved TEC retrieval based on spaceborne PolSAR data," *Radio Sci.*, vol. 53, no. 3, pp. 4022–4031, Dec. 2017.
[22] J. Li, Y. Ji, Y. Zhang, Q. Zhang, H. Huang, and Z. Dong, "A novel strategy of ambiguity correction for the improved Faraday rotation estimator in linearly full-polarimetric SAR data," *Sensors*, vol. 18, no. 4, p. 1158, Apr. 2018.
[23] F. J. Meyer and J. B. Nicoll, "Prediction, detection, and correction of Faraday rotation in full-polarimetric L-band SAR data," *IEEE Trans. Geosci. Remote Sens.*, vol. 46, no. 10, pp. 3076–3086, Oct. 2008.
[24] G. Sandberg, L. E. B. Eriksson, and L. M. H. Ulander, "Measurements of Faraday rotation using polarimetric PALSAR images," *IEEE Geosci. Remote Sens. Lett.*, vol. 6, no. 1, pp. 142–146, Jan. 2009.
[25] M. Jehle, M. Ruegg, L. Zuberbuhler, D. Small, and E. Meier, "Measurement of ionospheric Faraday rotation in simulated and real spaceborne SAR data," *IEEE Trans. Geosci. Remote Sens.*, vol. 47, no. 5, pp. 1512–1523, May 2009.
[26] J. S. Kim, K. P. Papathanassiou, R. Scheiber, and S. Quegan, "Correcting distortion of polarimetric SAR data induced by ionospheric scintillation," *IEEE Trans. Geosci. Remote Sens.*, vol. 53, no. 12, pp. 6319–6335, Dec. 2015.

YIFEI JI was born in Jiangyin, Jiangsu, China, in 1992. He received the B.S. degree in electronic information engineering from the Nanjing University of Science and Technology, Nanjing, in 2014, and the M.S. degree in information and communication engineering from the National University of Defense Technology (NUDT), Changsha, in 2016.

He is currently pursuing the Ph.D. degree with the College of Electronic Science, NUDT. His research interests include radar signal processing, synthetic aperture radar, and ionospheric impacts.

QILEI ZHANG was born in Gansu, China. He received the B.S. degree in communication engineering, and the M.S. and Ph.D. degrees in information and communication engineering from the National University of Defense Technology (NUDT), Changsha, in 2007, 2009, and 2014, respectively. From 2012 to 2013, he was a Visiting Ph.D. Student with the University of Birmingham, Birmingham, U.K.

He is currently a Lecturer with NUDT. His research interests include signal processing, synthetic aperture radar, and ionosphere.

YONGSHENG ZHANG was born in Inner Mongolia, China, in 1977. He received the Ph.D. degree in electronics and information engineering from the National University of Defense Technology (NUDT), in 2007.

He is currently an Associate Professor with the School of Electronic Science, NUDT. His current major research interests include SAR system design and SAR data processing.

ZHEN DONG was born in Anhui, China, in 1973. He received the Ph.D. degree in electrical engineering from the National University of Defense Technology (NUDT), Changsha, in 2001. He is currently a Professor with the School of Electronic Science and Engineering, NUDT.

His recent research interests include SAR system design and processing, ground moving target indication, and digital beamforming.

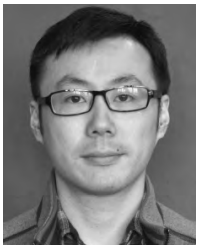

BAIDONG YAO was born in Anqing, China, in 1984. He received the B.S. degree in electronics engineering from Anhui University, Hefei, China, in 2006, and the Ph.D. degree in optics from the University of Chinese Academy of Sciences, China, in 2013.

Since 2013, he has been with the Earth Observation Research and Development Center, East China Research Institute of Electronic Engineering, where he was involved in performing the design of spaceborne SAR systems and more recently studying the design of spaceborne P-band SAR systems, P-band SAR applications, and ionospheric effects' correction methods.